GeoStorage

Vol. 1, No. 1, p. 71-79, 2025

Original article

A Zero-Pore-Pressure Slope Infiltrometer for Controlled Saturation and Accurate Hydraulic Conductivity Measurement

Mengxi Wu[1,2*], Shixiong Song[1], Zhenggang Zhan[3]

[1] *Institute of Mechanics, Chinese Academy of Sciences, Beijing 100190, China*
[2] *University of Chinese Academy of Sciences, Beijing 101408, China*
[3] *Powerchina Guiyang Engineering Corporation Limited, Guiyang 550081, China*

Keywords:
Field infiltration measurement
hydraulic conductivity
infiltrometers
slope stability
rainfall infiltration

Cited as:
Wu MX, Song SX, Zhan ZG, 2025. A Zero-Pore-Pressure Slope Infiltrometer for Controlled Saturation and Accurate Hydraulic Conductivity Measurement, GeoStorage, 1(1), 71-79.
https://doi.org/10.46690/gs.2025.01.05

Abstract:
Soil water infiltration fundamentally governs hydrological processes, yet existing measurement methods remain inadequate for slope conditions. This study presents a novel slope infiltrometer designed for precise infiltration measurements under saturated, zero-ponding conditions across 0°-42° slopes. The system combines Mariotte-controlled water supply with minimal soil disturbance (2 cm insertion depth), successfully characterizing silt to sandy soils (T1-T6 tests). Validation against TDR measurements demonstrated strong agreement, with absolute moisture content errors of -4.6% to +0.4% (83% of cases within ±11% relative error). Compared to conventional methods, the design eliminates surface pressure gradients while remaining insensitive to initial moisture conditions, enabling direct saturated hydraulic conductivity determination. The technique provides complete infiltration curves within 1-6 hours, offering significant advantages for hillslope hydrology studies and irrigation design under natural slope conditions.

1 Introduction

Soil water infiltration during rainfall governs surface runoff, groundwater recharge, and plant-available water storage (Lei et al., 1988; Bodhinayake et al., 2004; Casanova et al., 2000). Accurate infiltration measurement is essential for modeling storm floods, debris flows, and slope stability, which are critical for assessing the long-term geotechnical stability of above-ground infrastructure at underground fuel storage sites (Shi, 2019; Minasny and McBratney, 2000; Ogden et al., 1997; Peterson and Bubenzer, 1986). Furthermore, quantifying infiltration dynamics is paramount for the safety and efficiency of geostorage operations in caverns (e.g., underground water-sealed oil storage). Excessive or uneven infiltration can alter pore pressure in the overburden, potentially impacting the mechanical stability of the cavern roof and the sealing efficiency of the caprock (Li and Laloui, 2017; Jiang et al., 2011). It also governs the potential leaching of brines or hydrocarbons from surface evaporation ponds or accidental spills, which is a key environmental risk factor (Zhang et al., 2015). Therefore, the research on rainfall infiltration is not only of great significance for surface processes but also very important for the research of underground engineering.

While coupled soil-water-plant models have advanced since the 1990s, field measurement techniques remain limited, particularly for sloping terrains (Assouline et al., 2022). This is a significant gap, as strategic storage facilities are often located in hilly or coastal areas with complex topography. Existing methods include: Single-ring pressure infiltrometers (SRI) (Reynolds and Elrick, 1990), prone to flow divergence errors (Angulo-Jaramillo et al., 2016). Double-ring infiltrometers (DRI) (Bouwer, 1986), which disturb the natural soil structure and are unsuitable for non-horizontal surfaces (Levy et al., 1997). Tension infiltrometers (TI) (Perroux and White, 1988), sensitive to initial moisture content (Meshgi and Chui, 2014). Point-source methods (Mao et al., 2016), unsuitable

Yandy Scientific Press

* Corresponding author.
E-mail address: wumx@imech.ac.cn (Wu MX); ssx@imech.ac.cn (Song SX); zhanzg_gyy@powerchina.cn (Zhan ZG)

Received Jun. 18, 2025; revised Aug. 28, 2025; accepted Sep. 4, 2025; available online Sep. 13, 2025.

for slopes due to wetting-front ovalization. Lassabatere et al. (Lassabatere et al., 2019) highlighted the need for slope-adapted devices in heterogeneous soils. Zhang et al. demonstrated machine learning applications for coefficient of permeability K estimation but noted field-validation gaps (Zhang et al., 2018). Verschaffel et al. emphasized the role of microtopography in infiltration variability, unresolved by current tools (Verschaffel-Drefke et al., 2022).

Standard methods for estimating Drainage Rate Indexes (DRIs) and Transmissivity Indexes (TIs) assume horizontal ground surfaces. However, on slopes, pressure gradients caused by gravity alter flow paths, leading to significant measurement errors (Mamedov et al., 2001; Joel and Messing, 2000; Mao et al., 2011). Although some studies claim applicability up to 20% slopes (Bodhinayake et al., 2004), pressure head variations (upslope vs. downslope) yield relative rather than absolute results (Meshgi and Chui, 2014; Xu et al., 2002; Zhang et al., 2015). Excavation-based methods (Mendoza and Steenhuis, 2002) are destructive, impractical, and compromise the integrity of the site—an unacceptable risk for critical infrastructure like geostorage facilities (Alagna et al., 2016). This study introduces a novel slope infiltrometer that maintains zero water pressure across slopes, enabling direct K measurement without surface alteration or soil disturbance. This advancement provides a reliable and non-invasive tool for the accurate site characterization and long-term monitoring of near-surface hydrology around geostorage caverns, which is essential for risk assessment, stability analysis, and environmental protection.

2 Slope infiltrometer system

The primary objectives of surface infiltration measurements are to determine the saturated hydraulic conductivity (K_s) and saturated moisture content (θ_s) of soils. The slope infiltrometer developed in this study maintains a near-zero water pressure head uniformly across the entire slope surface, thereby resolving the inherent limitation of pressure heterogeneity observed in conventional double-ring (DRI) and tension infiltrometer (TI) methods.

2.1 Novel device

As illustrated in Fig. 1, the slope infiltrometer system comprises three integrated components: Mariotte water supply tanks, A dual-zone rainulator assembly and paired slope infiltration rings. This system achieves zero pore water pressure conditions through the coordinated operation of Mariotte tanks (Ankeny et al., 1988; Perroux and White, 1988) and a rainfall simulator (rainulator).The infiltration ring design follows the DRI principle, featuring an inner measurement ring concentrically positioned within an outer buffer ring. This arrangement ensures: unidirectional vertical flow within the measurement zone, exclusive data collection from the inner ring and hydraulic isolation from lateral flow effects

The rainulator incorporates two independent chambers (inner and outer) supplied by separate Mariotte tanks via dedicated feed tubes. Water distribution occurs through precision-calibrated porous rain boards, delivering controlled precipitation to their respective ring zones.

Each Mariotte tank system includes: a sealed main reservoir with top-fill inlet, a graduated borosilicate glass water-level measuring tube and an air intake tube with vent orifice positioned at surface elevation (lowest point within ring).

The system comprises five ring types (A-E) with unique slope ratios (vertical/horizontal). Each vertical ring has upper and lower edges, both serving as downward-facing sides for sloped terrain installation. The ten rims (two per type) show progressive 0.05:1 slope ratio increments between configurations (Fig. 2).

For slope surfaces up to 42.8° (slope ratio ≤0.925:1), the design ensures:

(1) Maximum slope ratio discrepancy between ring rim and soil surface: ≤0.025:1;

(2) Resultant maximum insertion depth variation: 0.625 cm for inner rings (0.025×25 cm); 1.25 cm for outer rings.

The operational hydraulic conditions includes:

(1) Maintains zero surface water pressure head;

(2) Ensures exclusively vertical downward seepage;

(3) Prevents upward water migration across ring boundaries.

The installation protocol outlines the minimal insertion depth requirements, which vary depending on the slope direction. For upslope contact, only a surface touch is necessary, while for downslope insertion, a depth of 2-3 cm is required. These specifications are in contrast to the DRI requirements, which mandate an insertion depth of 5-8 cm as specified.

The design advantages: Reduced wall thickness enhances stability during insertion, resulting in lower driving force requirements - a remarkable 60-70% reduction compared to DRI. Moreover, the design significantly minimizes soil disturbance owing to shallower insertion depths and thinner ring walls, ensuring a more efficient and environmentally friendly installation process.

2.2 Field infiltration dynamics and hydraulic regulation mechanisms

The infiltration test commences by supplying water from the dual Mariotte tanks to the rainulator. After securing the device on the target ground surface, the rainulator distributes water uniformly across both the inner and outer ring areas.

The system's hydraulic regulation occurs through the following sequence:

(1) Initial Ponding Phase: When valve opening causes rainfall intensity to exceed surface infiltration capacity, excess water accumulates at the ring's downslope end. Submerging the air tube vent establishes an airtight tank condition.

(2) Pressure Regulation Cycle: During water discharge in the airtight tank, air pressure gradually decreases in the tank headspace, reducing rainfall intensity ($\Delta P \approx 0.5-1.2 kPa/min$). Vent exposure during ponding recession breaks the airtight seal, and immediate pressure recovery restores higher rainfall intensity.

(3) Adaptive Rainfall Distribution: The system utilizes a strategic non-uniform rainfall pattern. This is achieved by incorporating graded pore sizing in the rain boards, with diameters ranging from 0.5 to 3 mm, and by implementing a progressive reduction in hole density, from 15-5 holes/cm² , as one moves from the upslope to the downslope.

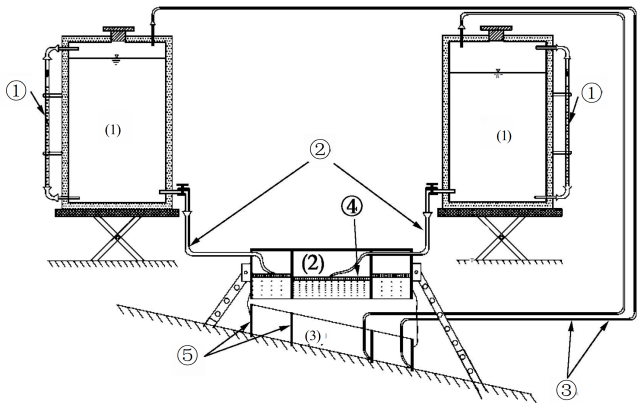

(1) Mariotte water tank; (2) Rainulator; (3) Double slope infiltration ring
① Borosilicate water-level tube; ② Delivery pipe; ③Air intake tube; ④Porous rain board; ⑤Slope infiltration ring

Fig. 1 Slope Infiltrometer – A saturated no-ponding slope surface infiltration test apparatus

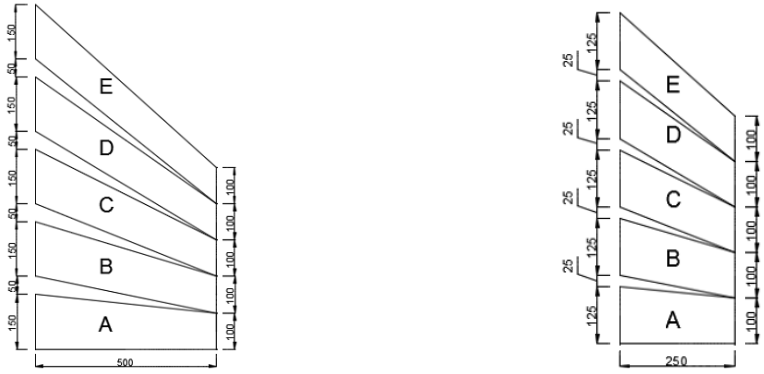

a b

Fig. 2 Geometry of infiltration ring (a) Outer ring, (b) Inner ring (in mm)

At equilibrium conditions, the average rainfall intensity $I_{avg} = K_{sat}$. This means that the upslope rainfall intensity $I_{up} > K_{sat}$, allowing for infiltration and potential runoff, while the downslope intensity $I_{down} = K_{sat}$, indicating that the soil is able to absorb all the falling rainwater without generating surface runoff.

The regulated hydraulic head induced unidirectional overland flow across the ring's internal surface along the imposed slope gradient (upper→lower edge), exhibiting three characteristic phases:

(1) Flow acceleration zone (upslope section): In this phase, the flow velocity increases to reach its peak at the mid-slope position. This acceleration is due to the gravitational force acting on the flow as it moves downslope, converting potential energy into kinetic energy

(2) Stable transport zone (mid-slope): Here, the flow maintains its maximum velocity. The energy input from the hydraulic head is balanced by energy losses due to friction and turbulence, resulting in a steady flow regime.

(3) Flow dissipation zone (lower 20% slope): In this final phase, the flow's kinetic energy is completely dissipated at the slope toe. Energy losses through friction, turbulence, and possibly interactions with the underlying surface cause the flow to slow down and come to rest.

This three-phase flow dynamic is characteristic of overland flow on a sloped surface and is influenced by factors such as slope gradient, surface roughness, and the hydraulic head.

During surplus conditions ($I_{avg} > K_{sat}$), the system achieves self-regulation through the following processes: ponding-induced vent causes a progressive reduction in rainfall intensity, which induces flow zone contraction from the slope toe and ultimately reduces I_{avg}.

Compensatory mechanisms are in place to offset local infiltration deficits, which are mitigated by:

(1) enhanced infiltration at the slope toe due to ponding;

(2) lateral redistribution of moisture;

(3) capillary-driven transverse seepage.

The automated vent transition mechanism ensures optimal surface saturation ($\psi = 0$) is maintained by dynamically matching the applied rainfall intensity to the soil's saturated infiltration capacity (K_{sat}) throughout the duration of the test.

2.3 Field testing procedure and data collection

The equipment should be set up by securing the infiltrometer in the test location and fully opening both water supply

valves to ensure complete surface coverage within the rings and controlled ponding at the downslope end. During the initial operation, continuous monitoring of the water level in Mariotte tanks with an accuracy of ±1 mm and the elapsed test time with a resolution of 1 second is required. Under zero pore water pressure conditions, the initial infiltration rates decrease rapidly, typically by 60-80% within the first 10 minutes, and stabilization occurs within 30-45 minutes, which may vary depending on the soil type. This corresponds to a reduction in rainfall intensity by 40-70% of the initial value. The valve adjustment protocol involves gradually reducing the valve opening in 25-50% increments based on observations of ponding depth, surface flow patterns, and real-time infiltration rate calculations.

2.4 Post-test measurements

The infiltration test protocol involves a systematic procedure for data acquisition, which includes recording the real-time water level in the tanks and the elapsed time. Subsequently, a plot of the cumulative infiltration versus time curve is generated to analyze the data effectively. Tab.1 shows the main post-test measurements.

Tab. 1 Post-Test Measurements

Parameter	Method	Precision
Total infiltration depth (z)	Core sampling (inner ring center), wetting front identification	±0.5 cm
θ_{sat}	TDR probe (8 cm) or gravimetric (100 cm^3)	–
$\theta_{initial}$	TDR probe or gravimetric (1 m reference)	–

Conversion formula for gravimetric (w) to volumetric (θ) moisture:

$$\theta = w \times \frac{\rho_b}{\rho_w} \tag{1}$$

where, ρ_b= bulk density (g/cm^3), ρ_w = water density ($1g/cm^3$)

3 Infiltration parameter calculations

Cumulative infiltration (Q) can be calculated:

$$Q = (\theta_{sat} - \theta_{initial}) \times z \tag{2}$$

Where Q is cumulative infiltration. Data sources for analysis and modeling can be derived from two primary methods: direct measurements and the Green-Ampt model parameter inversion.

3.1 Infiltration rate dynamics (v-t relationship)

Infiltration rates typically follow a distinct temporal pattern characterized by (i) an initial high-rate phase, (ii) a rapid decrease phase, and (iii) eventual stabilization near K_{sat}. This pattern represents the soil's maximum infiltration capacity under zero ponding pressure, with the initial phase influenced by surface-connected macropores and the final phase controlled by the soil matrix's saturated conductivity. Tab.2 listed the numerical differentiation methods.

Tab. 2 Numerical Differentiation Methods

Method	Error Characteristics	Applicability
Forward difference	Overestimates v (initial-phase bias)	Total infiltrated water per unit area
Backward difference	Underestimates v (lagging effect)	Emergency estimates
Central difference	Minimal error (gold standard)	Scientific-grade accuracy

The central difference formula for calculating v at time t_i:

$$v_i = \frac{Q_{i+1} - Q_{i-1}}{t_{i+1} - t_{i-1}} \quad (i = 2, 3, 4, \ldots) \tag{3}$$

where i refers to the sequence number of the data recorded.

3.2 Hydraulic principles of the slope infiltrometer method

The slope infiltrometer induces one-dimensional vertical seepage through the soil column within the inner ring. This phenomenon occurs because, under saturated conditions, the water pressure at the soil surface equals zero, which is equivalent to atmospheric pressure. As a result, the driving hydraulic gradient ($\frac{\nabla h}{\nabla L}$) is solely determined by gravitational potential, which plays a crucial role in dictating the direction and rate of water flow through the soil column. This simplified condition allows for the precise measurement and analysis of soil hydraulic properties using the slope infiltrometer.

$$\Delta h/\Delta L = \Delta z/\Delta z = 1 \tag{4}$$

where Δz is the elevation head difference and ΔL is the flow path length. This configuration typically results in a sharp wetting front that clearly demarcates the saturated zone ($\theta \approx \theta_s$) from the unsaturated zone ($\theta = \theta_0$), a phenomenon consistently observed in field studies (Lassabatere et al., 2019; Verschaffel-Drefke et al., 2022). This physical process aligns perfectly with the fundamental assumptions of the Green-Ampt infiltration model(Green and Ampt, 1911).

The Green-Ampt Formulation model represents the wetting front as a distinct boundary, characterized by a discontinuity in moisture content. Specifically, above the front, the soil is saturated, denoted by $\theta = \theta_s$, while below the front, the soil maintains its initial moisture content, indicated by $\theta = \theta_0$. This conceptualization highlights the sharp transition in soil moisture conditions across the wetting front, which is crucial in understanding and predicting water movement and distribution in the soil profile.

For one-dimensional saturated infiltration, the cumulative infiltration Q relates to wetting front depth z by:

$$Q = \int_0^t [\theta_0(z) - \theta_0(z)]\, dz \tag{5}$$

where z is the depth of the wetting front (the distance between the ground surface and the wetting front).

The instantaneous infiltration rate v is given by:

$$v = k_{sat}\{1 + [h + h_a(z)]/z\} \quad (6)$$

where,K_{sat} is the saturated hydraulic conductivity; h is the surface water pressure head;h_a refers to the soil suction below the wetting front.

Under zero pressure head ($h = 0$), Eq.6 simplifies to:

$$v = k_{sat}\ [1 + h_a(z)/z] \quad (7)$$

This establishes an inverse proportionality between v and z when h_a is constant, producing a linear v vs. $1/z$ relationship.

3.3 Experimental determination of parameters

The $z - Q$ relationship derives from measured Q-t curve and Eq.5.

Water content difference $\Delta\theta = \theta_s - \theta_0$

While surface conditions (0-20 cm depth) often exhibit $\Delta\theta$ variability due to evaporation and vegetation effects, the effective $\Delta\theta$ can be precisely determined as:

$$\theta_s - \theta_0 = Q_{final}/Z_{final} \quad (8)$$

where Q_{final} and Z_{final} are total values at test termination.

The derived relationships include:

(1) the z-t curve, which is obtained by combining the Q-t measurements with Eq.5;

(2) the v-t curve, calculated through numerical differentiation of the Q-t data;

(3) the v-z relationship, established by parametrically eliminating t.

Fig. 3 presents the characteristic v-1/z relationship observed in slope infiltrometer tests. The data reveal a distinct linear regime when $1/z < 4\ m^{-1}$ (corresponding to infiltration front depths $z > 0.25$ m). This linear behavior can be explained by two key factors:

(1) Moisture Content Stabilization: While the initial moisture content (θ_0) shows significant depth-dependence in shallow layers ($z \leq 0.25$ m), it asymptotically approaches a constant value at greater depths.

(2) Capillary Pressure Equilibrium: Similarly, the capillary pressure head at the wetting front (h_a) becomes effectively constant beyond this depth threshold.

These conditions satisfy the theoretical requirement of Eq. 7.

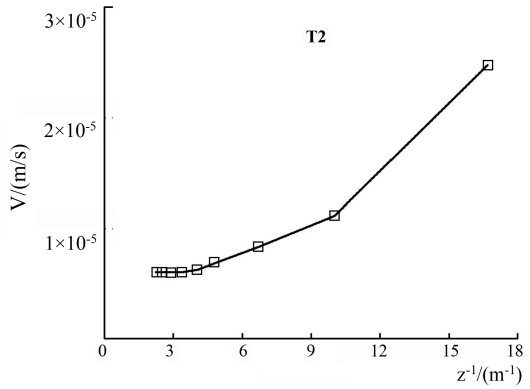

Fig. 3 Typical v–1/z curve in a slope infiltraometer test

The linear segment of the measured v-1/z curve (Fig. 3) can be fitted through linear regression to determine the soil's hydraulic properties. The y-intercept of the best-fit regression line corresponds to the saturated hydraulic conductivity (K_{sat}t), while the slope represents the product of K_{sat} and the capillary pressure head (h_a). This approach provides a straightforward yet robust method to simultaneously estimate both k_{sat} and h_a from a single test, in contrast to conventional methods that require complicated unsaturated flow modeling. The slope infiltrometer technique maintains good accuracy even under low initial saturation conditions ($\theta_0 < 0.3$), where alternative methods often yield unreliable estimates of saturated hydraulic conductivity, as the constant (h_a) and θ_0 values at greater depths satisfy the theoretical assumptions of the linear relationship. The method's effectiveness derives from its direct measurement of infiltration dynamics and the self-stabilizing nature of deeper wetting fronts.

4 Field test and parameter regression

We conducted field infiltration measurements in a 400 km^2 mountainous catchment in Qamdo, Tibet from July 7-14, 2015. Six test sites (Fig. 4) were established across varying terrain conditions:

(1) Slope gradients: 5-30°;

(2) elevations: 2659-4128 m ASL;

(3) Soil types: silt, silty sand, or sand.

The experimental setup (Fig. 5) employed a slope infiltrometer to measure cumulative infiltration versus time in the inner ring. Post-infiltration, we measured:

The soil moisture content was measured using an 8-cm TDR probe. Saturated conditions were determined by readings taken from the center of the inner ring, while initial conditions were established with a reference point located 100 cm away. Vertical insertion of the probe provided an average value for soil moisture (θ) in the 0-8 cm depth, avoiding the need for destructive horizontal measurements. To determine the infiltration depth, 1-m core samples (34mm ID geotome) were collected from the center of the inner ring. The wetting front position was then identified visually.

The infiltration depth is calculated as follows: Infiltration

depth equals the total sample length minus the dry portion length.

This methodology balanced measurement accuracy with field practicality in challenging alpine conditions.

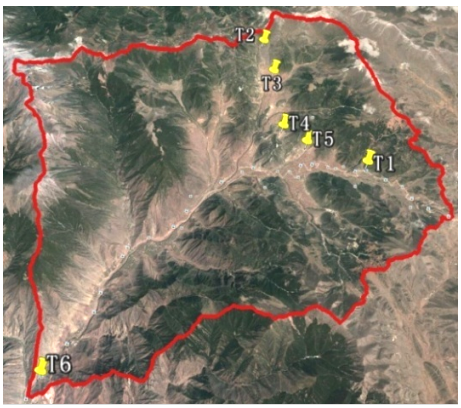

Fig. 4 Six positions for field infiltration tests

Fig. 5 The slope infiltrometer at the test field

Tab. 3 Site-Specific Soil Properties

Test	Slope (°)	Soil Profile Description	Surface Condition
T1	5	Red silty sand (USSC: SM)	50% grass cover (2 cm height)
T2	21	Red silt (ML) with 2 cm dark brown subsurface horizon	50% grass cover (2 cm height)
T3	30	Gravelly agricultural silt (GM-ML)	Dry crust over moist layer (>4 cm)
T4	17	Cemented silty soil (CL) with 5% gravel content	Extremely dry (15 cm penetration resistance >4 MPa)
T5	20	Meadow silt (ML)	Dense root mat (0-10 cm)
T6	20	Sandy gravel (GP-GM)	30-40% gravel surface coverage

USSC: Unified Soil Classification System

5 Infiltration observations using 34mm ID geotome

Figs. 6 and 7 display the total infiltration volume (Q_A) as a function of time and illustrate both cumulative infiltration (Q) and instantaneous infiltration rate ($v = dQ/dt$) temporal trends for all test conditions, respectively.

Characteristic infiltration phases:

During the initial phase, which lasted from 0 to 30 minutes, all soil types displayed notably high initial infiltration rates, with rates exceeding 100 mm/h. Subsequently, a rapid rate decay was observed, aligning with power-law kinetics, as denoted by t - n, where the value of n ranged between 0.5 and 0.8.

During the stabilization phase (>90 min), quasi-steady infiltration rates (v_∞) were achieved within 90-120 minutes. Terminal infiltration capacities varied significantly across different soil types.

Tab. 4 Main parameters of each test period

Test	Stabilized Rate (mm/h)	Relative to T1 (%)
T1	47.4 ± 2.1	100 (reference)
T2	23.4 ± 1.8	49.4
T3	80.8 ± 3.5	170.5
T4	5.4 ± 0.9	11.4
T5	13.4 ± 1.2	28.3
T6	51.1 ± 2.7	107.8

The key findings indicate significant differences in infiltration capacity and terminal rates among various soil conditions. Specifically, gravel-containing soil (T3) exhibited a 71% higher infiltration capacity compared to the reference bare soil (T1). In contrast, surface crusting (T4) led to a remarkable 88.6% reduction in terminal rates relative to T1. Additionally, grass cover (T2) resulted in a 50.6% decrease in stabilized infiltration rates when compared to bare soil conditions. These findings highlight the impact of soil composition and surface characteristics on water infiltration processes.

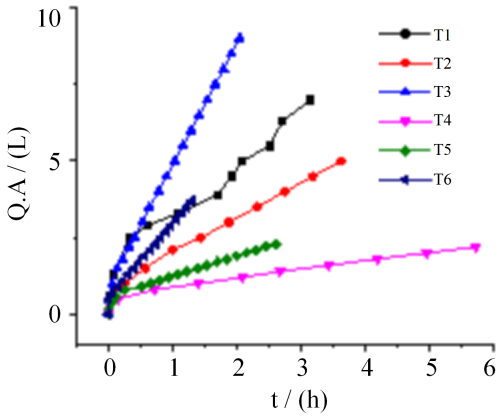

Fig. 6 Six positions for field infiltration tests

Fig. 8 illustrates the v-1/z relationship obtained from two sources:

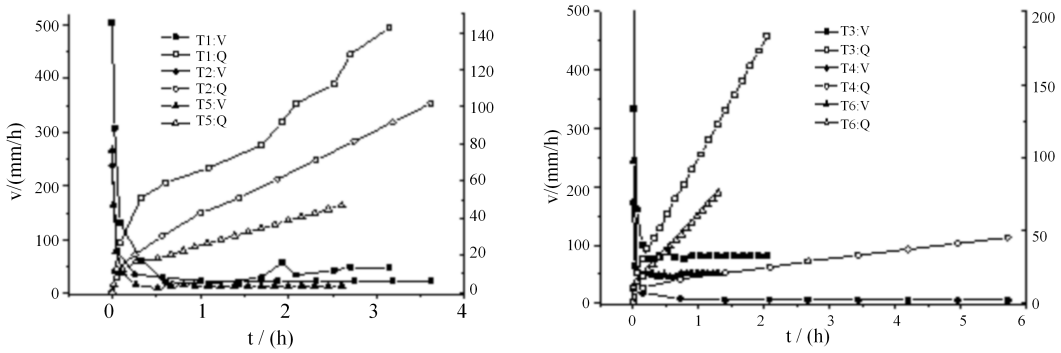

a b

Fig. 7 Infiltration rate (v) and cumulative infiltration (Q) vs. time

(1) final infiltration depth measurements

(2) cumulative infiltration-time curves (v-t) acquired using a slope infiltrometer.

The methodology involved applying linear regression to the quasi-linear segment of the v-1/z curve (Fig. 9). This regression provided two important parameters: the intercept, representing saturated hydraulic conductivity (k_{sat}), and the slope, which is associated with soil suction (h_a).

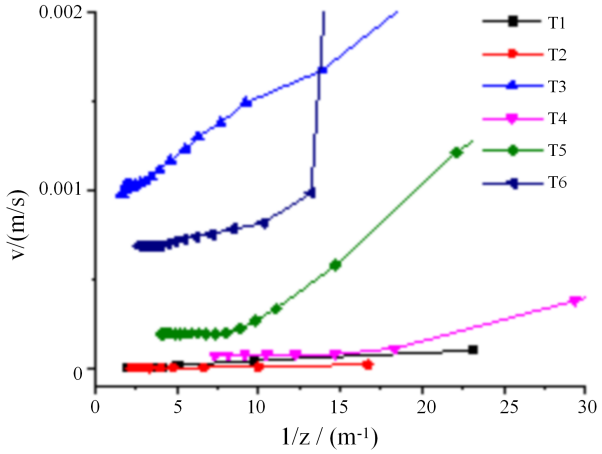

Fig. 8 v-1/z curve

The results showed that the soil suction characteristics ranged from a minimum of 0.3 cm to a maximum of 6.8 cm across all tests, with the complete data presented in Tab. 3. The terminal slope analysis, as depicted in Fig. 6 Q-t curves, revealed that the slopes descended in the order of T3 > T6 > T1 > T2 > T5 > T4. Notably, the corresponding $k_(sat)$ values maintained the same ranking as observed in the terminal slopes, which is detailed in Tab. 3.

By conducting error analysis, we discovered that the strong correlation (R_2 > 0.95) between terminal Q-t curve slopes and saturated hydraulic conductivity confirms:

Higher infiltration rates at stabilization phase directly indicate greater k_{sat} values.

Tab. 5 Saturated hydraulic conductivities, suctions and corresponding depth ranges

Test No.	$k_s \times 10^{-6}$ m/s	ha/cm
T1	7.19	6.8
T2	5.75	2.1
T3	18.8	4.7
T4	1.40	1.6
T5	3.97	0.3
T6	13.5	1.4

6 Method validation and reliability assessment

To validate the performance of the proposed slope infiltrometer system, we conducted a dual-measurement approach that included:

(1)Infiltration parameters obtained from the slope infiltrometer.

(2)Independent soil moisture monitoring using time-domain reflectometry (TDR, Model XYZ, with ±2% accuracy).

The validation is based on the fundamental soil physics relationship:

$$Q/z = \theta_{\text{sat}} - \theta_{\text{iniinal}} = \Delta\theta \quad (9)$$

where Q is cumulative infiltration (L); z is wetting front depth (cm), and $\Delta\theta$ is moisture content difference.

The key findings of the study are as follows: The maximum absolute error observed was 0.046 m³/m³, specifically for measurement point T4, while the minimum absolute error was 0.000 m³/m³ at point T5. Furthermore, 83% of the measurements demonstrated agreement within a ±10% margin.

An analysis of error sources in TDR measurements reveals variability within a nominal accuracy of ±2%. Additionally, there is uncertainty in wetting front detection of ±0.5 cm, and soil heterogeneity at the measurement scale contributes to potential errors.

The strong agreement between the methods (R_2 = 0.89) confirms robust performance under various slope conditions (5°-30°), reliable determination of saturated hydraulic conductivity, and accurate characterization of the infiltration process.

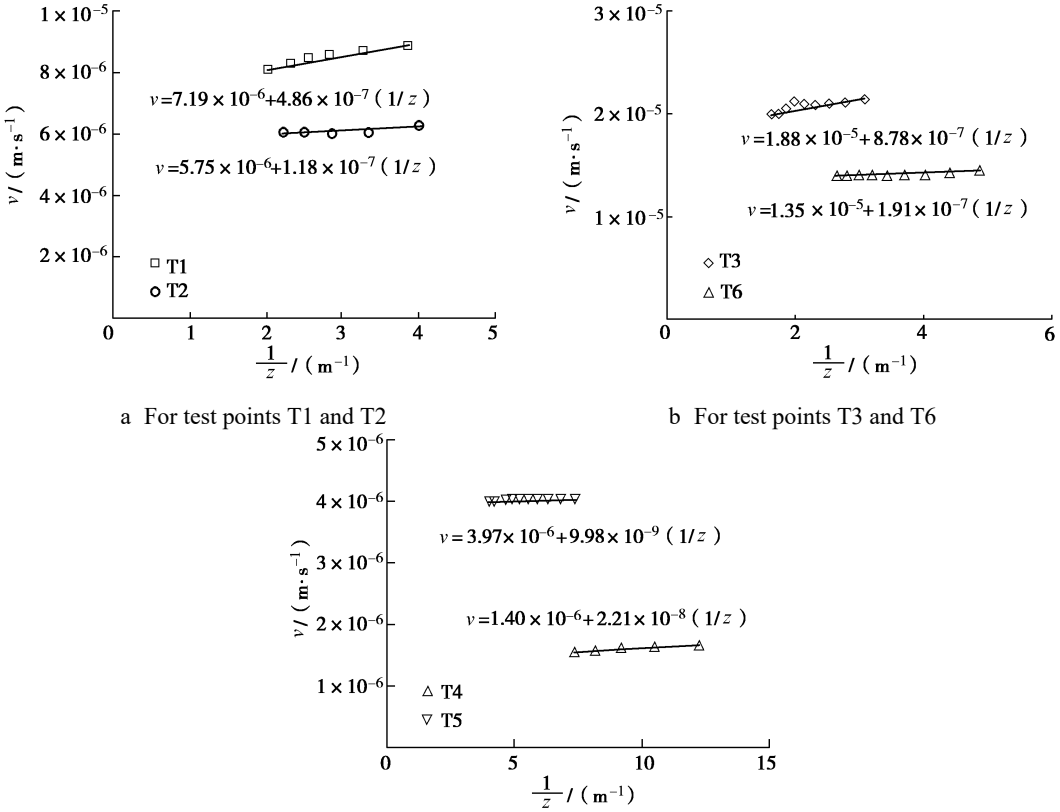

a For test points T1 and T2

b For test points T3 and T6

c For test points T4 and T5

Fig. 9 Linear regression of v-1/z curve

Tab. 6 Moisture content validation results

No.	Infiltration	TDR measured			Total infiltration	Measured infiltration	Calculated $\Delta\theta$	Error%	Relative
	duration/h	θ_0	θ_s	$\Delta\theta$	volume/L	depth/cm			error%
T1	3.23	0.135	0.373	0.238	7	55	0.259	-2.1	-8.1
T2	3.71	0.165	0.355	0.190	5	50	0.204	-1.4	-6.9
T3	2.14	0.123	0.375	0.252	9	65	0.282	-3.0	-10.6
T4	5.62	0.074	0.327	0.253	2.2	15	0.299	-4.6	-15.4
T5	2.30	0.175	0.355	0.180	2.3	26	0.180	0.0	0.0
T6	1.22	0.067	0.259	0.192	3.7	40	0.188	0.4	2.1

Acknowledgements

This work was supported by Huaneng Lancang River Science and Technology Project Grant No.HNKJ15-H13

Conflict of interest

The authors declare no competing interest.

References

Alagna V, Bagarello V, Prima SD, et al. 20176. Determining hydraulic properties of a loam soil by alternative infiltrometer techniques. *Hydrology Processes*, **30**(2): 263–275. doi: 10.1002/hyp.10607.

Ankeny MD, Kaspar TC, Horton R. 1988. Design for an automated tension infiltrometer. *Soil Science Society of America Journal*, **52**(3): 893–896. doi: 10.2136/sssaj1988.03615995005200030054x.

Angulo-Jaramillo R, Bagarello V, Iovino M, et al. 2016. *Infiltration Measurements for Soil Hydraulic Characterization*. Springer. doi:10.1007/978-3-319-31788-5.

Assouline S, Narkis K, Or D. 2022. Evaporation from soils under thermal boundary conditions: Experimental and modeling investigation. *Water Resources Research*, **58**, e2021WR031161. doi:10.1029/2021WR031161.

Bodhinayake W, Si BC, Xiao CJ. 2004. New Method for Determining Water-Conducting Macro- and Mesoporosity from Tension Infiltrometer. *Soil Science Society of America Journal*, **68**(3): 760-769. doi:10.2136/sssaj2004.7600.

Bodhinayake W, Si BC, Noborio K. 2004. Determination of hydraulic properties in sloping landscapes from tension and double-ring infiltrometers. *Vadose Zone Journal*, **3**(3): 964-970. doi: 10.2136/vzj2004.0964.

Bouwer H. 1986. Intake Rate: Cylinder Infiltrometer. In: Klute,

A. (Ed.), *Methods of Soil Analysis, Part 1. Physical and Mineralogical Methods*. American Society of Agronomy, Madison, WI, pp. 825–843. doi:10.2136/sssabookser5.1.2ed.c32.

Casanova M, Messing I, Joel A. 2000. Influence of aspect and slope gradient on hydraulic conductivity measured by tension infiltrometer. *Hydrological Processes*, **14**(1): 155–164.

Green WH. Ampt GA. 1911. Studies in soil physics. I. The flow of air and water through soils. *Journal of Agricultural Science*, **4**(1): 1–24. doi: 10.1017/S0021859600001441.

Jiang ZM, Zeng L, Zhao HB, et al. 2011. Numerical study on variation features of water table in area of underground rock cavern for oil storage. *Chinese Journal of Geotechnical Engineering*, **33**(11): 1780-1785. doi:10.1016/j.gete.2017.06.003.

Joel A, Messing I. 2000. Application of two methods to determine hydraulic conductivity using disc permeameters on sloping land. *European Journal of Soil Science*, **51**(1): 93–98. doi:10.1046/j.1365-2389.2000.00281.x

Lei ZD, Yang SX, Xie SC. 1988. *Soil Physics*. Tsinghua University Press, pp. 77–78.

Levy GJ, Levin J, Shainberg I. 1997. Prewetting rate and aging effect on seal formation and interrill soil erosion. *Soil Science*, **162**(2): 131–139. doi: 10.1097/00010694-199702000-00006.

Li C, Laloui L. 2017. Impact of material properties on caprock stability in CO_2 geological storage. *Geomechanics for Energy and the Environment*, **11**: 28–41. doi:10.1016/j.gete.2017.06.003.

Lassabatere L, Prima SD, Angulo-Jaramillo R, et al. 2019. Beerkan multi-runs for characterizing water infiltration and spatial variability of soil hydraulic properties across scales. *Hydrological Sciences Journal*, **64**(2): 165-178. doi: 10.1080/02626667.2018.1560448.

Mamedov AI, Levy GJ, Shainberg I, et al. 2001. Wetting rate and soil texture effect on infiltration rate and runoff. *Soil Research*, **39**(6), 1293–1305. doi: 10.1071/SR01029.

Mao LL, Lei TW, Bralts VF. 2011. An analytical approximation method for the linear source soil infiltrability measurement and its application. *Journal of Hydrology*, **411**(3-4), 169–177. doi: 10.1016/j.jhydrol.2011.08.066.

Mao LL, Li YZ, Hao WP, et al. 2016. An approximate point source method for soil infiltration process measurement. *Geoderma* **264**, 10–16. doi: 10.1016/j.geoderma.2015.09.011.

Mendoza G, Steenhuis TS. 2002. Determination of hydraulic behavior of hillsides with a hillslope infiltrometer. *Soil Science Society of America Journal*, **66**(5): 1501-1504. doi: 10.2136/sssaj2002.1501.

Meshgi A, Chui TFM. 2014. Analysing tension infiltrometer data from sloped surface using two-dimensional approximation. *Hydrological Processes*, **28**(3): 744–752. doi:10.1002/hyp.9621.

Minasny B, McBratney AB. 2000. Estimation of sorptivity from disc-permeameter measurements. *Geoderma*, **95**(3–4), 305–324. doi: 10.1016/S0016-7061(99)00096-8.

Ogden CB, ES HM, Schindelbeck RR. 1997. Miniature rain simulator for measurement of infiltration and runoff. *Soil Science Society of America Journal*, **61**(4): 1041–1043. doi: 10.2136/sssaj1997.03615995006100040008x.

Perroux KM, White I. 1988. Design for disc permeameters. *Soil Science Society of America Journal*, **52**(5): 1205–1215. doi: 10.2136/sssaj1988.03615995005200050001x.

Peterson, A.E., Bubenzer, G.D., 1986. Intake Rate: Sprinkler Infiltrometer. In: Klute A. (Ed.), *Methods of Soil Analysis, Part 1. Physical and Mineralogical Methods*, American Society of Agronomy, Madison, WI, pp. 784–810. doi: 10.2136/sssabookser5.1.2ed.c33.

Reynolds D, Elrick D. 1990. Ponded Infiltration From a Single Ring: Analysis of Steady Flow. *Soil Science Society of America Journal*, **54**(5): 1233-1241. doi: 10.2136/sssaj1990.03615995005400050006x.

Shi L. 2019. Study on the characteristics and appropriateness of artificial water-sealed function for underground storage cavern in rainfall area (Doctoral Dissertation). Beijing: China University of Geosciences (Beijing).

Verschaffel-Drefke C, Balzer C, Schedel M, et al. 2022. Experiment for validation of numerical models of coupled heat and mass transfer around energy cables. *Vadose Zone Journal*, **21**(1), e20173. doi: 10.1002/vzj2.20173.

Xu MX, Liu GB, Bu CF, et al. 2002. Experimental study on soil infiltration characteristics using disc permeameter. *Transactions of the Chinese Society of Agricultural Engineering (Transactions of the CSAE)*, **18**(4), 54-58.

Zhang XF, Liu WC, Su ZY, et al. 2015. Characteristics of polutants from underground storage tank leakage in social gas station in Chengdu plain. *Environmental Engineering*, **33**(7): 127-130. doi:10.13205/j.hjgc.201507028.

Zhang Y, Schaap MG, Zha YY. 2018. A high-resolution global map of soil hydraulic properties produced by a hierarchical parameterization of a physically based water retention model. *Water Resources Research*, **54**(12): 9774-9790. doi:10.1029/2018WR023539.